# Formation of stratospheric nitric acid by a hydrated ion cluster reaction: Implications for the effect of energetic particle precipitation on the middle atmosphere

O.-K. Kvissel,[1] Y. J. Orsolini,[2] F. Stordal,[1] I. S. A. Isaksen,[1] and M. L. Santee[3]

Received 1 December 2011; revised 2 July 2012; accepted 2 July 2012; published 17 August 2012.

[1] In order to improve our understanding of the effects of energetic particle precipitation on the middle atmosphere and in particular upon the nitrogen family and ozone, we have modeled the chemical and dynamical middle atmosphere response to the introduction of a chemical pathway that produces $HNO_3$ by conversion of $N_2O_5$ upon hydrated water clusters $H^+\cdot(H_2O)_n$. We have used an ensemble of simulations with the National Center for Atmospheric Research (NCAR) Whole-Atmosphere Community Climate Model (WACCM) chemistry-climate model. The chemical pathway alters the internal partitioning of the $NO_y$ family during winter months in both hemispheres, and ultimately triggers statistically significant changes in the climatological distributions of constituents including: i) a cold season production and loss of $HNO_3$ and $N_2O_5$, respectively, and ii) a cold season decrease and increase in $NO_x/NO_y$-ratio and $O_3$, respectively, in the polar regions of both hemispheres. We see an improved seasonal evolution of modeled $HNO_3$ compared to satellite observations from Microwave Limb Sounder (MLS), albeit not enough $HNO_3$ is produced at high altitudes. Through $O_3$ changes, both temperature and dynamics are affected, allowing for complex chemical-dynamical feedbacks beyond the cold season when the pathway is active. Hence, we also find a $NO_x$ polar increase in spring-to-summer in the southern hemisphere, and in spring in the northern hemisphere. The springtime $NO_x$ increase arises from anomalously strong poleward transport associated with a weaker polar vortex. We argue that the weakening of zonal-mean polar winds down to the lower stratosphere, which is statistically significant at the 0.90 level in spring months in the southern hemisphere, is caused by strengthened planetary waves induced by the middle and sub-polar latitude zonal asymmetries in $O_3$ and short-wave heating.

**Citation:** Kvissel, O.-K., Y. J. Orsolini, F. Stordal, I. S. A. Isaksen, and M. L. Santee (2012), Formation of stratospheric nitric acid by a hydrated ion cluster reaction: Implications for the effect of energetic particle precipitation on the middle atmosphere, *J. Geophys. Res.*, *117*, D16301, doi:10.1029/2011JD017257.

## 1. Introduction

[2] Nitric acid ($HNO_3$) is considered to be a very important chemical species in the stratosphere. As a key reservoir for the reactive nitrogen ($NO_x$), $HNO_3$ intervenes in the nitrogen-dominated ozone ($O_3$) depleting cycle, and it plays an important role in the halogen-dominated catalytic cycle leading to polar $O_3$ depletion. For these reasons, the distribution of $HNO_3$ in the stratosphere has been studied closely with ground-based and satellite instruments. In the last two decades, a large amount of observations from several satellite-borne instruments, such as the Limb Infrared Monitor of the Stratosphere Experiment (LIMS) on the NIMBUS 7, the Sub-Millimeter Radiometer (SMR) aboard Odin, the Michelson Interferometer for Passive Atmospheric Sounding (MIPAS) aboard ENVISAT, the Microwave Limb Sounder (MLS) aboard UARS and Aura, and the High Resolution Dynamics Limb Sounder (HIRDLS) also aboard Aura, has allowed the distribution of $HNO_3$ in the stratosphere to be characterized [*Gille et al.*, 1984; *Santee et al.*, 2004; *Stiller et al.*, 2005; *Kinnison et al.*, 2008; *Orsolini et al.*, 2009; *Urban et al.*, 2009].

[3] The primary chemical source of $HNO_3$ is the three-body gas-phase reaction between the hydroxyl radical (OH) and nitrogen dioxide ($NO_2$), while its major sinks are photolysis and oxidation by OH. While $HNO_3$ peaks in the winter lower stratosphere at high latitudes, enhanced abundances of $HNO_3$ are commonly observed in the polar mid and upper stratosphere, as revealed by ground-based [*de Zafra et al.*, 1997; *McDonald et al.*, 2000] and satellite observations [*Austin et al.*, 1986; *Kawa et al.*, 1995; *Orsolini et al.*, 2005; *Stiller et al.*, 2005; *López-Puertas et al.*, 2005;

[1]Department of Geosciences, University of Oslo, Oslo, Norway.
[2]Norwegian Institute for Air Research, Kjeller, Norway.
[3]Jet Propulsion Laboratory, California Institute of Technology, Pasadena, California, USA.

Corresponding author: O.-K. Kvissel, Department of Geosciences, University of Oslo, NO-0315 Oslo, Norway. (o.k.kvissel@geo.uio.no)


0148-0227/12/2011JD017257

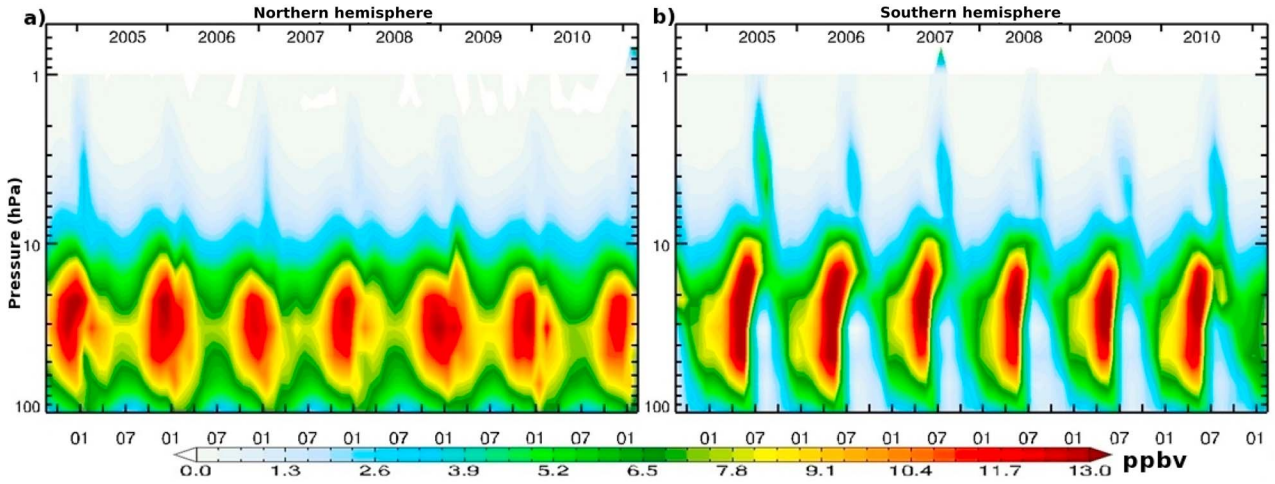


**Figure 1.** Time versus pressure evolution of $HNO_3$ (ppbv) averaged poleward of 70° in the (a) northern and (b) southern hemispheres, from August 2004 to February 2011, based on monthly means from MLS version 3.3. In this and in all following figures with time on the *x* axis, the tick marks indicate the middle of the month.

*Orsolini et al.*, 2009]. Figure 1 shows the monthly evolution of $HNO_3$ (averaged poleward of 70° in each hemisphere) observed by Aura/MLS (data version 3.3; see Appendix A) from August 2004 to February 2011. Descending tongues of $HNO_3$-enriched air are apparent above 10 hPa during winter in both hemispheres above the main $HNO_3$ layer between approximately 100 and 10 hPa, which leads to a secondary maximum in the $HNO_3$ profile between 10 and 1 hPa.

[4] The intensity of these recurring $HNO_3$ enhancements between 10 and 1 hPa varies from year to year and appears stronger in the southern hemisphere (SH), where enhanced mixing ratios can reach approximately 6 ppbv. Up to the stratopause, the vertical extent of $HNO_3$ is comparable in both hemispheres. These MLS observations are in overall agreement with other instruments, as polar-averaged daily values ranging from 5 to 10 ppbv were reported between 25 and 40 km by SMR [*Orsolini et al.*, 2009] and MIPAS [*Orsolini et al.*, 2005; *López-Puertas et al.*, 2005]. Note that the early winter disappearance of the $HNO_3$ below about 30 hPa in the SH corresponds to the beginning of the polar stratospheric cloud (PSC) formation period, when uptake from the gas phase chemistry exists. In the northern hemisphere (NH) some discontinuities linked to stratospheric sudden warmings occur when the vortex undergoes weakening and displacement.

[5] Enhancement of mid and upper stratospheric $HNO_3$ is believed to be linked to a high-altitude source of $NO_x$. Energetic particle precipitation (EPP) can create $NO_x$ in situ in the upper stratosphere during solar proton events (SPEs), via the so-called EPP/$NO_x$ "direct" effect [*Jackman et al.*, 2005, 2008; *Randall et al.*, 2006, 2009; *Semeniuk et al.*, 2011]. Upper-stratospheric $NO_2$ enhancements (above 100 ppbv) linked to EPP events have occasionally been observed [e.g., *Callis and Lambeth*, 1998; *Orsolini et al.*, 2005; *López-Puertas et al.*, 2005]. SPEs can induce a rapid $HNO_3$ enhancement lasting for a few days at altitudes of approximately 40 km and above, as observed during the strong SPEs of November 2001, October 2003 and January 2005 [*Orsolini et al.*, 2009; *Verronen et al.*, 2008, 2011]. Complex ion reactions have been proposed to foster these $HNO_3$ enhancements immediately following SPEs [*Verronen et al.*, 2008, 2011].

[6] Besides in situ stratospheric production, $NO_x$ enhancements can arise from the descending flux of $NO_x$-rich air through the stratopause in the winter polar regions, the so-called EPP/$NO_x$ "indirect" effect. $NO_x$ is produced in the mesosphere and thermosphere during the pervasive low energy auroral electron precipitation, or during more sporadic and higher energy electron precipitation events. Recurrent $HNO_3$ enhancements are associated with the EPP/$NO_x$ "indirect" effect; however, the production of $NO_x$ as well as the efficiency of the mesosphere-to-stratosphere transport exhibits some variability, especially in the more dynamically active NH. Heterogeneous conversion of dinitrogen pentoxide ($N_2O_5$) to $HNO_3$ upon hydrated ion clusters [*Böhringer et al.*, 1983; *Kawa et al.*, 1995] has been suggested as a probable explanation for the slower enhancements following the EPP/$NO_x$ "indirect" effect. In this case, the anomalously large $NO_x$ concentration leads to excess $N_2O_5$ and then to the increased production of $HNO_3$ by conversion of $N_2O_5$ on hydrated water cluster ($H^+ \cdot (H_2O)_n$):

$$\text{(R1)} \qquad N_2O_5 + H^+ \cdot (H_2O)_n \rightarrow H^+ \cdot (H_2O)_{n-1} + 2HNO_3.$$

[7] In the lower stratosphere, heterogeneous conversion of $N_2O_5$ on sulfate aerosols could also play a significant role in producing $HNO_3$ [e.g., *Bekki et al.*, 1997; *de Zafra and Smyshlyaev*, 2001].

[8] The high-altitude EPP-related source of $HNO_3$ is not well accounted for in stratospheric chemistry-transport models (CTM), or in middle atmosphere chemistry-climate models (CCM) as these models do not include the relevant ion chemistry. An exception to the former case is the recent study by *Reddmann et al.* [2010], who incorporated the ion cluster reaction (R1) into a chemistry-transport model. Focusing on the stratospheric $NO_x$ and $HNO_3$ descent following the SPEs of October 2003, the $HNO_3$ abundance in

their model improved significantly with the inclusion of the afore mentioned reaction. Going beyond the study with prescribed stratospheric dynamics by *Reddmann et al.* [2010], in this paper we use a free-running CCM, which can produce coupled responses in both chemistry and dynamics. To this end, we use the Whole-Atmosphere Community Climate Model (WACCM) to investigate the role of reaction (R1) in the formation of $HNO_3$ enhancements through the $NO_x$ indirect effect, and more generally its impact on the year-round evolution of stratospheric chemistry. We use an ensemble approach to study the primary chemical effects of the reaction as well as secondary effects due to combined, coupled changes in chemistry and dynamics. The model and the experimental setup are presented in Section 2, whereas the main results are presented in Section 3. Section 4 briefly addresses some of the biases in WACCM, and a discussion and a summary are provided in Section 5.

## 2. Modeling Methodology

### 2.1. Whole-Atmosphere Community Climate Model (WACCM)

[9] We use version 3.1.9 of WACCM developed at the National Center for Atmospheric Research (NCAR) [*Garcia et al.*, 2007]. WACCM covers the vertical region from the surface up to $6.0 \times 10^{-6}$ hPa (equivalent to approximately 130 km geometric altitude) with 67 hybrid sigma-pressure levels. We have run WACCM with a horizontal resolution equivalent to $1.9^\circ \times 2.5^\circ$ (latitude $\times$ longitude) and a time step of 1800 s for the physical parameterizations; this time step is further subdivided as necessary to ensure computational stability. WACCM incorporates a detailed neutral advection and chemistry model for the middle atmosphere, including heating due to chemical reactions; a model of ion chemistry in the mesosphere/lower thermosphere (MLT); ion drag and auroral processes; and parameterizations of shortwave heating at extreme ultraviolet wavelengths and infrared transfer under nonlocal thermodynamic equilibrium conditions. The WACCM chemistry module is derived from the three-dimensional chemical transport Model for OZone And Related chemical Tracers version 3 (MOZART-3) described in *Brasseur et al.* [1998] and (http://gctm.acd.ucar.edu/gctm/mozart). It solves numerically 51 neutral species, including all the significant members of the $O_x$, $NO_x$, $HO_x$, $ClO_x$ and $BrO_x$ chemical families and respective reservoir species. Tropospheric source species such as $N_2O$, $CH_4$, $H_2O$, chlorofluorocarbons (CFCs) and other halogenated compounds are included. Heterogeneous processes on sulfate aerosols and polar stratospheric clouds (liquid binary sulfate, supercooled ternary solutions, nitric acid trihydrate, and water ice), as well as aerosol sedimentation, are represented. The photolysis rates in WACCM for all absorbing species are calculated interactively. Further details regarding photolytic reaction rates and the chemistry module in general are given in *Kinnison et al.* [2007].

### 2.2. Model Setup

[10] To investigate the impact of $HNO_3$ formation by heterogeneous chemistry on hydrated ion clusters, we ran WACCM for 4 successive years. A simulation with an additional effective chemical reaction mimicking (R1) ("perturbed simulation" detailed below) is compared with a control simulation without this reaction. Prescribed climatological sea surface temperatures were used, but the solar forcing and surface emissions correspond to the years 1998 to 2002. Since our aim is to model $HNO_3$ enhancements due to the EPP/$NO_x$ "indirect" effect, individual SPEs are not introduced as forcing in our simulations. The diagnostics presented in this paper were carried out after a spin-up period of 6 months.

[11] Since WACCM is a free-running CCM, the interannual dynamical variability can be large. To minimize this internal variability, we used an ensemble approach in which we ran 4 pairs of 4-year control and perturbed simulations. This provides a total of 16 modeled years for each of the perturbed and control simulations. These 4 control and perturbed pairs (i.e., ensemble members) are initiated from different initial conditions, lagged by a day. Except in section 3.1, we only present ensemble-mean results with the statistical significance estimated by the standard Student t-test.

[12] Monthly mean distributions of minor species are interpreted with the aid of the Transformed Eulerian Mean (TEM) circulation. The total mass-weighted meridional circulation is calculated using monthly averaged dynamical fields. To represent the forcing of the TEM circulation by the resolved waves, we calculated the divergence of the Eliassen-Palm flux (EPFD), also using monthly averaged fields.

### 2.3. Additional $HNO_3$ Chemistry Introduced in WACCM

[13] The rate of the chemical reaction (R1) converting $N_2O_5$ to $HNO_3$ is controlled by the amount of $N_2O_5$ and $H^+\cdot(H_2O)_n$ available. Following *de Zafra and Smyshlyaev* [2001], we treated the reaction as a pseudo first-order reaction with a rate constant $k_p = k_2(H^+\cdot(H_2O)_n)$ where $k_2 = 3.5 \times 10^{-10}$ cm$^3$ s$^{-1}$, yielding

$$\frac{d(HNO_5)}{dt} = -2\frac{d(N_2O_5)}{dt} = 2k_p(N_2O_5).$$

[14] There is some uncertainty in the value of the $k_2$ constant. Based on *Böhringer et al.* [1983], *de Zafra and Smyshlyaev* [2001] give a range of $8.0 \times 10^{-10} < k_2 < 4.0 \times 10^{-12}$. We used $k_2 = 3.5 \times 10^{-10}$ cm$^3$ s$^{-1}$ near the upper limit, as suggested by *de Zafra and Smyshlyaev* [2001]. The reaction, in which one $N_2O_5$ molecule is lost and two $HNO_3$ molecules are produced, is processed in the implicit chemical solver for both species. The reaction has a side reaction consuming water vapor to regenerate the hydrated water cluster. However, this secondary effect was neglected here since it contributes as a marginal sink for stratospheric water vapor.

[15] We introduced a prescribed meridional distribution of hydrated water cluster $H^+\cdot(H_2O)_n$ shown in Figure 2, corresponding approximately to the distribution shown in Figure 5a from *Beig et al.* [1993]. The prescribed time-independent distribution depends upon latitude and height, and is symmetrical around the equator. The densities peak near 4000 molec/cm$^3$ at polar latitudes and are tapered to zero at 30°N or S. Under normal conditions, galactic cosmic rays are the primary source of ions in the stratosphere. While varying with geomagnetic latitude and moderately influenced by the 11-year solar cycle and large magnetic storms,

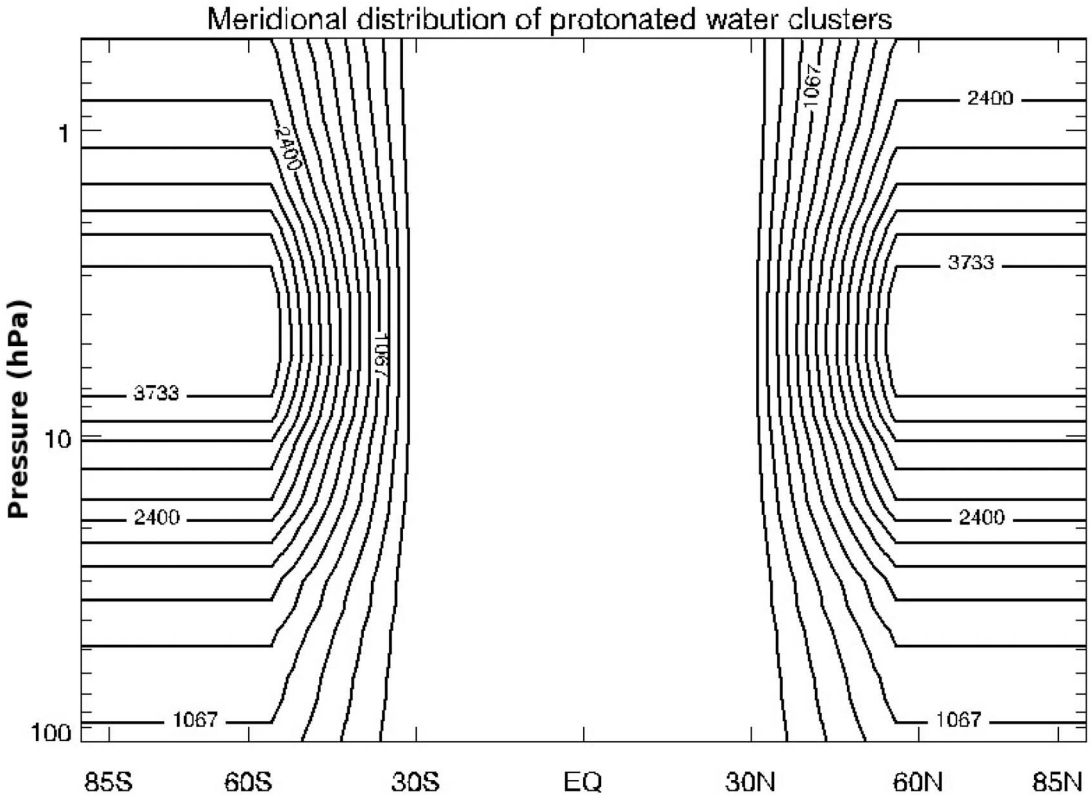


**Figure 2.** Prescribed meridional distribution of the density (molec /cm$^3$) of hydrated water cluster, $H^+ \bullet (H_2O)_n$, adapted from *Beig et al.* [1993].

the ion distribution exhibits relatively little short-term variation [*de Zafra and Smyshlyaev*, 2001]. As such, the use of a time-independent distribution of ion clusters serves as a good first order approximation.

## 3. Simulation Results

### 3.1. Primary Chemical Response in $N_2O_5$ and $HNO_3$

[16] Figure 3 shows the time evolution of differences in $HNO_3$ and $N_2O_5$ (averaged poleward of 70° in both hemispheres) between the perturbed and the control simulations over the pressure range 100–0.5 hPa. While we will display 4-member ensemble means in the rest of the paper, we show in Figure 3 the 4-yearlong simulation for a particular member to demonstrate the recurring conversion of $N_2O_5$ to $HNO_3$ in the mid-stratosphere in any given simulation. The corresponding distributions from the control simulation are also shown as dashed contour lines. A recurrent annual $HNO_3$ increase in the perturbed simulation appears when and where $N_2O_5$ is present. $N_2O_5$ is only abundant in the polar regions during the cold and dark season, i.e., during October to February in the NH, and April to August in the SH, when its thermal decomposition and photochemical conversion are slow. The magnitude of $HNO_3$ enhancements in the perturbed simulation are up to 6 ppbv near 20 hPa. In both hemispheres, the recurrent increase in $HNO_3$ in the perturbed simulation, around 30–10 hPa, is found above the maximum volume mixing ratio (vmr) in the control simulation. While the increase coincides in time with the winter maximum in the NH, its occurrence is after the seasonal maximum in the SH. In the lower stratosphere, differences in $HNO_3$ vary both in magnitude and sign interanually and are more pronounced in the SH. This characteristic was also evident in the other ensemble members. Such year-to-year differences are only marginally seen in $N_2O_5$.

[17] Figure 4 shows the climatological annual cycle of $HNO_3$ in both hemispheres, averaged poleward of 70°, for Aura/MLS (Figures 4a and 4b) based on monthly averages from the years 2004–2011, and for WACCM as an ensemble-mean based on monthly averages from 16 simulated years (Figures 4c and 4d: perturbed simulation, and Figures 4e and 4f: control simulation). The inclusion of the ion cluster reaction significantly improves the $HNO_3$ distribution throughout the year, especially in the SH (Figures 4b, 4d and 4f). The wintertime high-altitude abundance above 10 hPa, albeit improved, remains clearly lower than MLS, as the $HNO_3$ enhancements in WACCM do not extend as high as those measured by MLS or by SMR [e.g., *Verronen et al.*, 2011; *Orsolini et al.*, 2009]. In addition, the implementation of reaction (R1) has better aligned the model seasonal cycle with the observations above 10 hPa. In the NH (Figures 4a, 4c and 4e), the control simulation showed a warm season maximum, but the perturbed simulation now reveals a winter maximum, as observed by MLS. Below about 30 hPa however, $HNO_3$ is already overestimated in the control simulation compared to MLS, and the introduction of the pathway further increases this high bias. Although not included in the model, the MLS $HNO_3$ data also include the effects of solar proton events, e.g., in January 2005 (NH), September 2005 (SH), and December 2006 (NH).

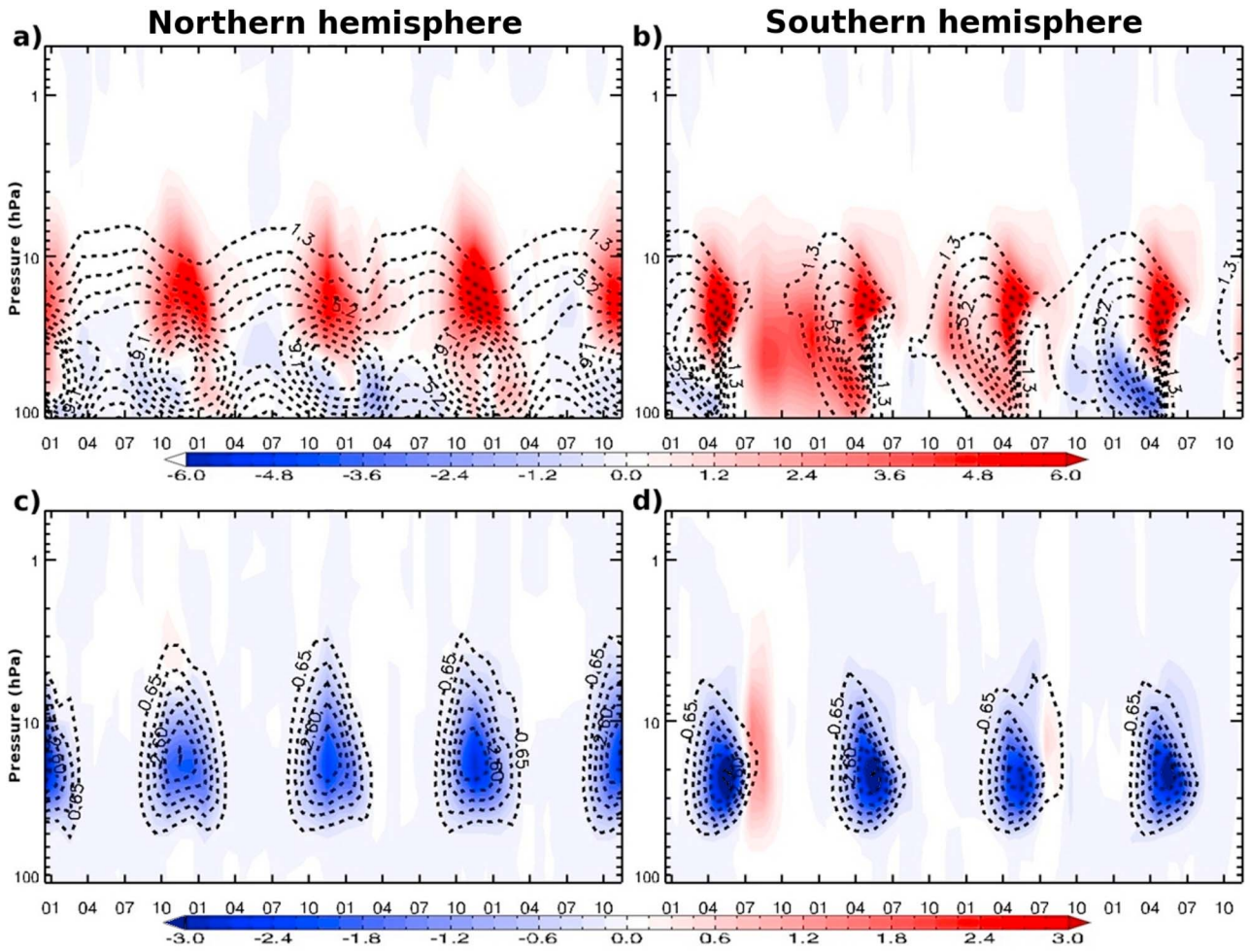


**Figure 3.** Time versus pressure evolution of the differences (perturbed minus control, color shaded) in (a, b) $HNO_3$ (in ppbv) and (c, d) $N_2O_5$ (in ppbv) for one ensemble member over the four simulated years (1999–2002), and averaged over polar regions (poleward of 70°) in the (left) northern and (right) southern hemispheres. Overlaid as dashed contour lines are the corresponding fields in the control simulation.

[18] The large occasional enhancements of $HNO_3$ in the lower stratosphere in the perturbed simulations, as in the first year in Figure 3b, can be explained by a spring break-up of the austral vortex. Such a break-up would lead to a poleward flux of $HNO_3$ from midlatitudes, where in fact $HNO_3$ is more abundant than at high latitudes [e.g., *Urban et al.*, 2009], due to permanent removal of $HNO_3$ by sedimentation of polar stratospheric cloud particles in winter. When the break-up occurs in late spring or summer, the meridional gradient of $HNO_3$ has waned, and it leaves a weak signature in $HNO_3$. We will return in Section 4 to the issues of potential WACCM biases and the impact of our assumptions regarding the background ion cluster distribution. In that section, we will relate the lack of high-altitude $HNO_3$ formation to a lack of available $N_2O_5$ in WACCM, and the high $HNO_3$ bias in the lower stratosphere to an excessive winter descent.

### 3.2. Response in $NO_x$, $N_2O$ and $O_3$

[19] The distributions of $O_3$ and $NO_x$ are governed by chemistry as well as transport processes. The competition between these two processes differs in various regions and seasons, and we will use the ratio of $NO_x/NO_y$ to separate these processes. The difference in this ratio between the perturbed and the control simulations will deviate from zero (positively or negatively) if chemistry alters the $NO_x$ abundance. Figure 5 shows the climatological annual cycle of the ensemble-mean difference between perturbed and control simulations, for $NO_x$, $NO_x/NO_y$-ratio and $O_3$ in the polar regions. The figure includes contours of statistical significance at the 0.9 and 0.75 levels. The corresponding ensemble-mean annual cycle from the control simulation is overlaid as dashed contours.

[20] We begin by describing the $NO_x$ and $NO_x/NO_y$-ratio (Figures 5a–5d). Between approximately 5 and 50 hPa, the introduced re-partitioning within the nitrogen family induces a clear deficit in the $NO_x/NO_y$-ratio during the cold season when $N_2O_5$ is available and R1 is active. This is due to the fact that $HNO_3$ is a longer-lived reservoir for $NO_x$, and the regeneration of $NO_x$ has slowed down. The polar-averaged deficit in $NO_x/NO_y$-ratio begins in the autumn in both hemispheres and is strongest during early and late winter - characteristics that are more salient in the SH.

[21] We infer that the $NO_x$ positive anomalies in regions where the $NO_x/NO_y$-ratio difference is close to zero (e.g., in

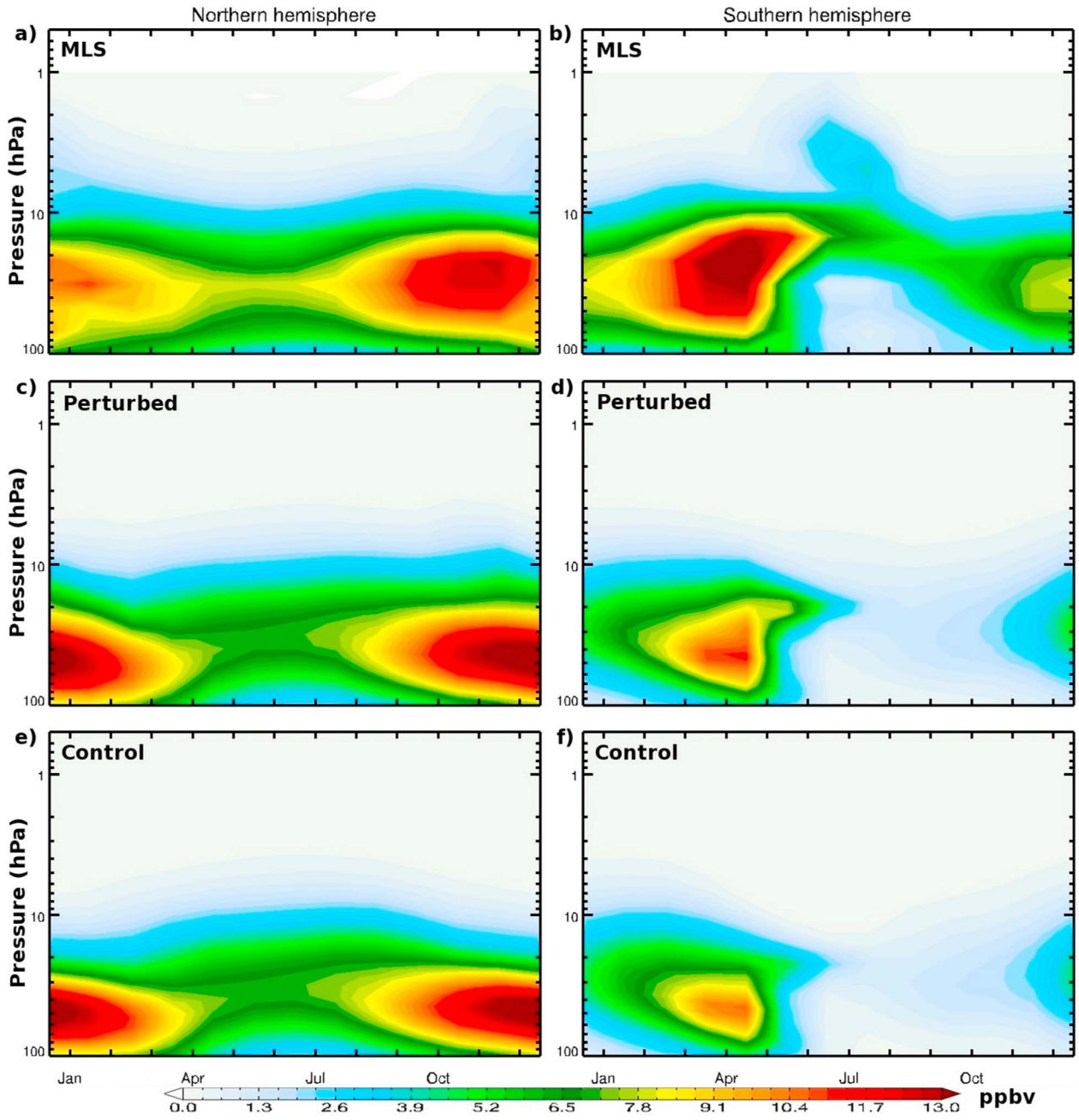


**Figure 4.** Climatological annual cycle of $HNO_3$ (ppbv) versus pressure, based on (a, b) monthly mean MLS data from 2004 to 2011, (c, d) ensemble mean from the WACCM perturbed simulation and (e, f) control simulation. Left and right columns show polar regions (poleward of 70°) in the northern and southern hemispheres, respectively.

the NH spring above 25 hPa, and in the SH winter, spring and summer above 50 hPa) are caused by transport and not by the direct influence of nitrogen chemistry. To further elucidate the origin of these anomalies, we examine in Figures 6a and 6b the climatological annual cycle of the ensemble-mean differences between the two simulations at 10 hPa as polar stereographic maps (40°–90° N in Figure 6a, and 40°–90° S in Figure 6b), for $N_2O$, $NO_x$, $O_3$, and $NO_x/NO_y$-ratio. While Figure 6 shows every other month, the auxiliary material Figures S1a and S1b show the entire seasonal cycle.[1] Ensemble-mean 10-hPa geopotential height differences are overlaid on the $N_2O$ panels, while ensemble-mean geopotential height for the control and the perturbed simulations are shown on the $O_3$ and $NO_x/NO_y$ panels, respectively. Figures 6a and 6b nicely show the annual cycle of the anomalies in $NO_x$ (or in $NO_x/NO_y$), with a pronounced high-latitude deficit in the cold season. Polar,

[1]Auxiliary material files are available in the HTML. doi:10.1029/2011JD017257.

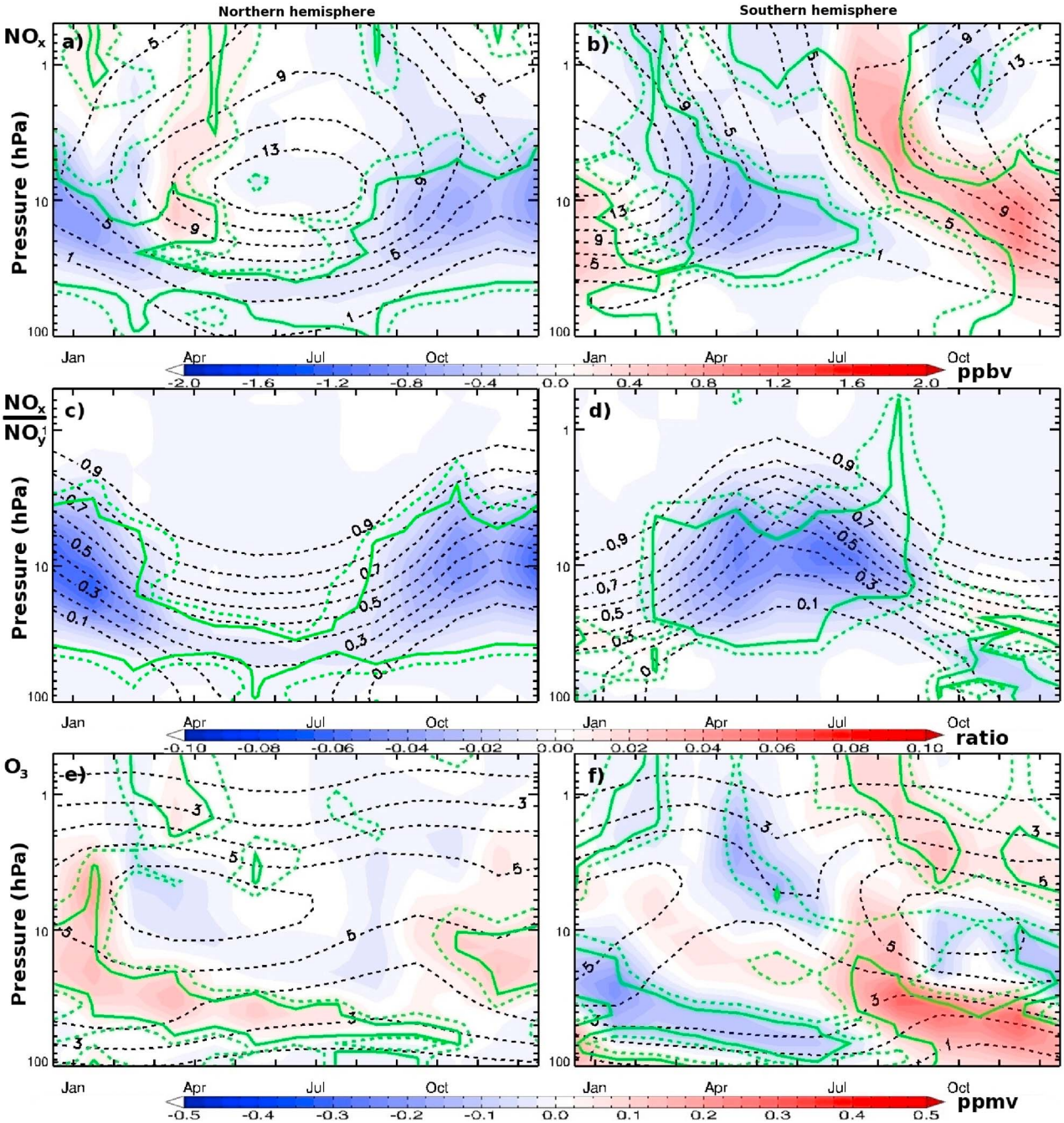


**Figure 5.** Climatological annual cycle of the ensemble mean differences (perturbed minus control, color shaded) in $NO_x$ (ppbv), $NO_x/NO_y$ ratio and $O_3$ (ppmv), averaged over polar regions (poleward of 70°) in the (a, c, e) northern and (b, d, f) southern hemispheres. Overlaid as dashed contour lines are the corresponding ensemble-mean fields in the control simulation. Significance at the 0.9 and 0.75 levels is indicated by the solid and dashed green contours, respectively.

positive $N_2O$ anomalies are evident from late winter to summer in the SH, and in spring in the NH, correlated with anomalies in geopotential height. Such positive correlations between $N_2O$ and geopotential height reflect the enhanced poleward transport from the $N_2O$-rich lower latitudes in a weakened polar vortex. As $N_2O$ is photochemically converted into NO in the sunlit spring and summer, a concomitant increase in $NO_x$ occurs. In the SH, the positive anomalies in $NO_x$ and $N_2O$ are both stronger in magnitude and more prolonged, lasting well into the summer season (e.g., Figures 6a and 6b, first two rows).

[22] The perturbed run with its stronger poleward advection in spring and summer has in fact brought the WACCM annual climatological cycle of $N_2O$ closer to MLS observations. This is demonstrated in Figure 7, which is the analogue of Figure 4 for $N_2O$. In the control simulation, in the

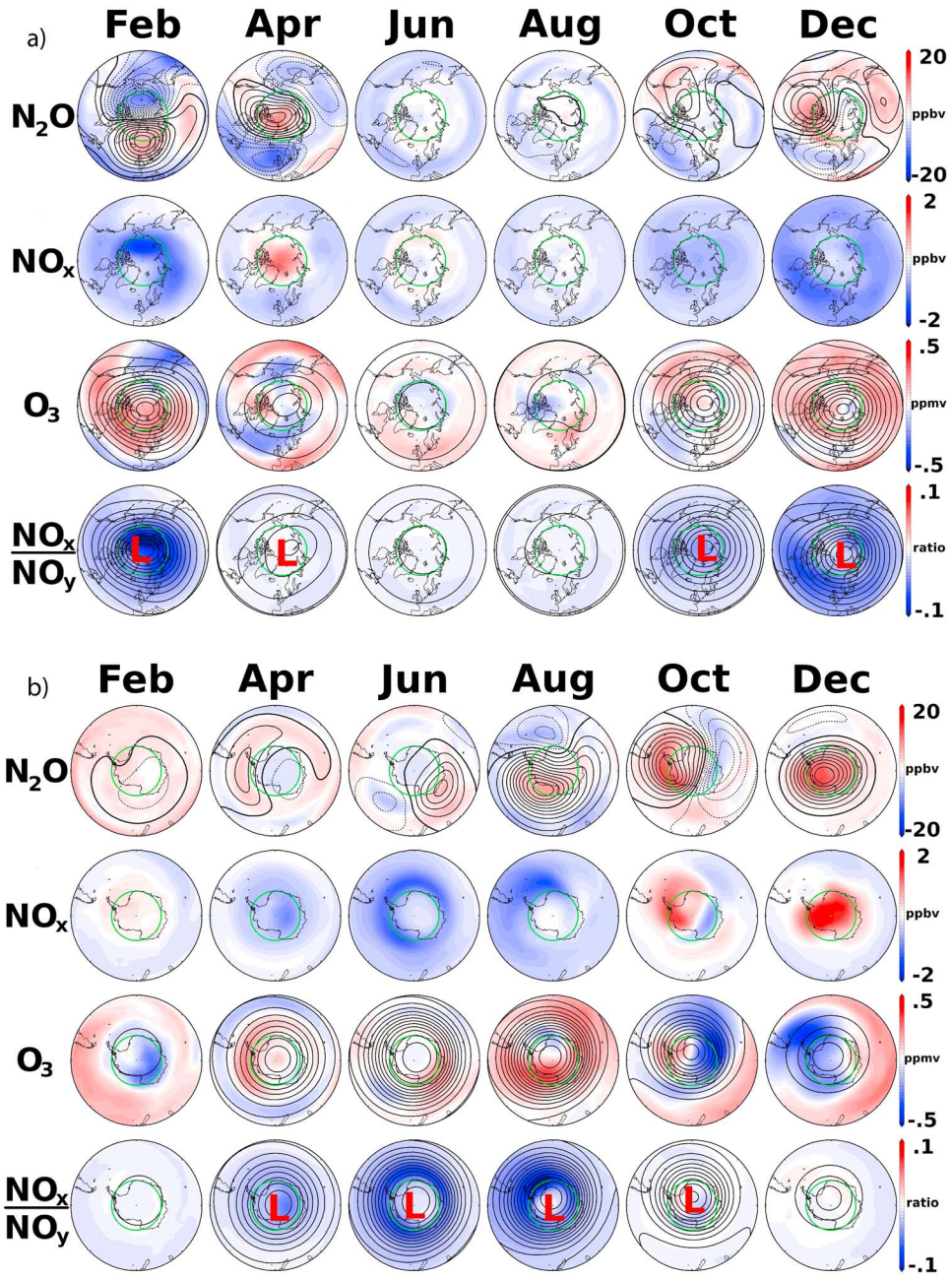


**Figure 6.** (a) Climatological annual cycle of the ensemble-mean difference (perturbed minus control, color shaded) for $N_2O$ (ppbv), $NO_x$ (ppbv), $O_3$ (ppmv) and the $NO_x/NO_y$-ratio at 10 hPa. Overlaid as black contour lines on $N_2O$ maps are the corresponding ensemble-mean geopotential height differences, with dashed and solid being negative and positive values, respectively. Overlaid as black contour lines on $O_3$ and $NO_x/NO_y$-ratio maps are the corresponding ensemble-mean geopotential heights from the control and perturbed simulation, respectively. Contour interval is 160 m for geopotential height and 20 m for geopotential height differences. Capital L and H indicate Low (geopotential height minimum) and High (geopotential height maximum) from the perturbed simulation. Polar (40°–90° N) stereographic maps, with green circle drawn at 70°N. (b) Same as in Figure 6a but for southern hemisphere (40°–90° S). The contour intervals of geopotential height and geopotential height differences are 320 m and 40 m, respectively.

SH in particular, the late spring and summer polar abundances were too low and peaked too late compared to MLS. The perturbed run has higher abundances and a steeper seasonal increase, albeit still smaller than in the observations. This is likely due to a tendency of this WACCM version to produce an austral polar vortex that is too long-lived, remaining climatologically strong until January (Figure 6b, third or fourth row). This would inhibit the poleward

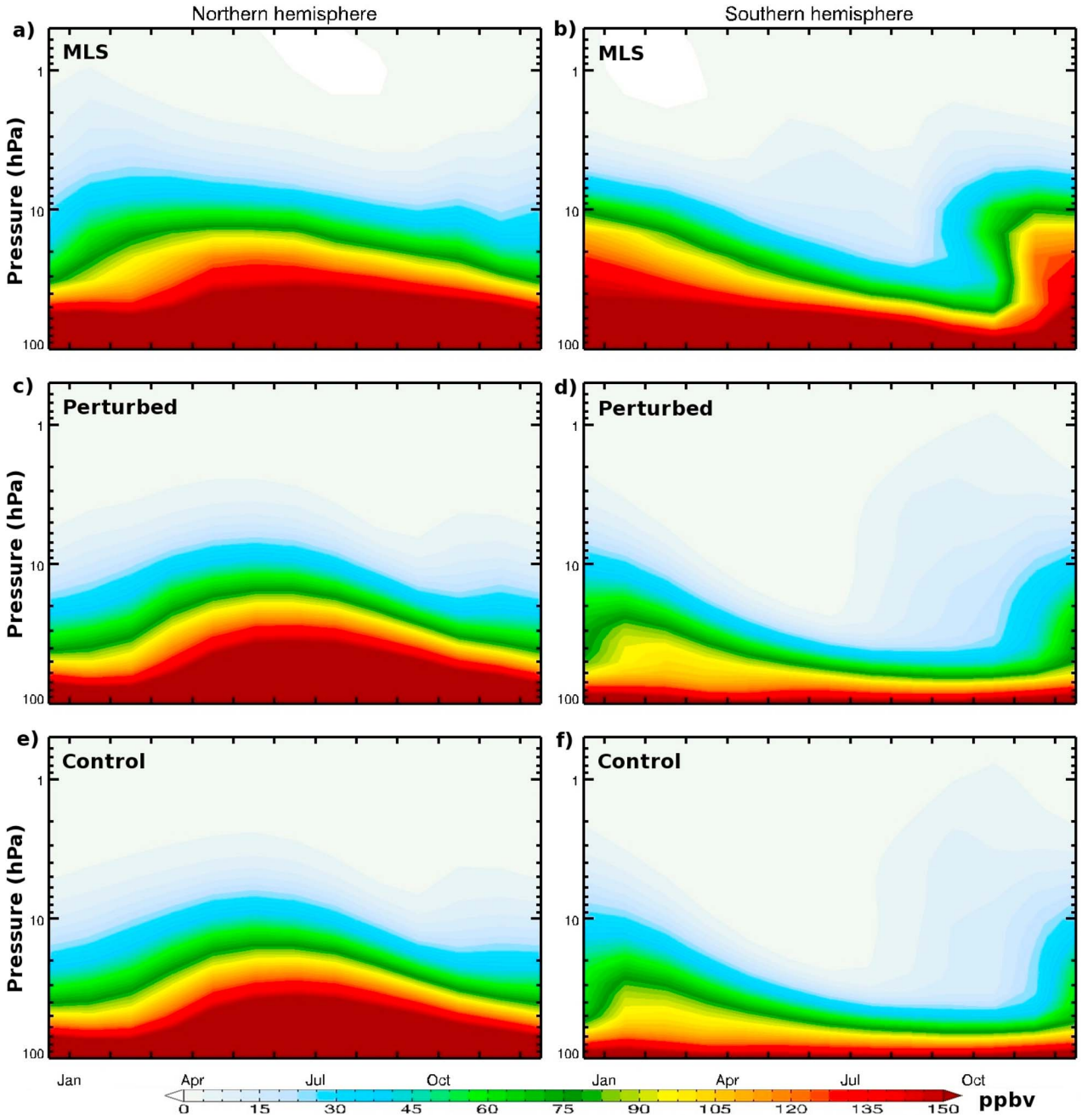


**Figure 7.** Climatological annual cycle of $N_2O$ (ppbv) versus pressure, based on (a, b) monthly mean MLS data from 2004 to 2011, (c, d) ensemble mean from the WACCM perturbed simulation and (e, f) control simulation. Left and right columns show the polar regions (poleward of 70°) in the northern and southern hemispheres, respectively.

transport of $N_2O$ rich air toward high latitudes. The earlier vortex weakening would also tend to alleviate the low $N_2O$ bias in the control run. Because MLS data only covers the years 2004–2011, the observed higher abundances in the NH winter above 30 hPa could reflect the occurrences of several major stratospheric sudden warmings in years 2004, 2006, 2009 and 2010 [e.g., *Orsolini et al.*, 2010; *Manney et al.*, 2008], which would bring $N_2O$-rich air from lower latitudes poleward. The SSWs would not occur at the same frequency in these WACCM runs.

[23] In summary, in the perturbed case, a pattern of decreased $NO_x$ abundance during winter is evident. The weaker spring vortex allows for a stronger poleward transport of $N_2O$, which translates into positive $NO_x$ anomalies, stronger and longer lasting in the SH. The recurrent spring and summer $NO_x$ excess in the mid-stratosphere is perhaps the most striking and unanticipated chemical anomaly arising from dynamical-chemical feedbacks, as it occurs when the cold-season ion cluster reaction (R1) is not active anymore.

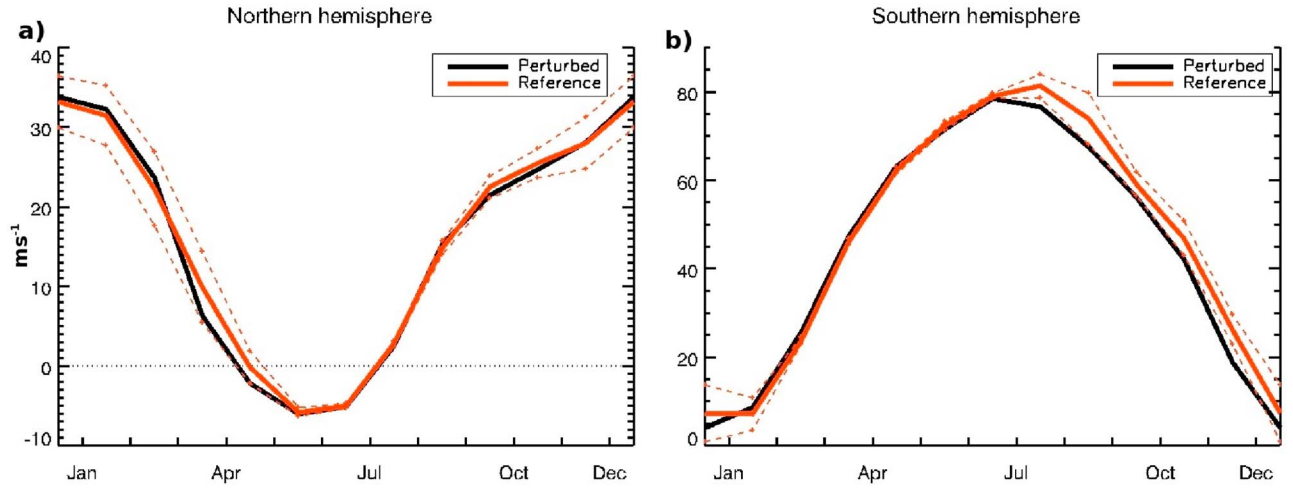


**Figure 8.** Climatological annual cycle of the monthly zonal-mean zonal wind at 10 hPa for the perturbed (black) and control (red) ensemble means, averaged over latitudes between (a) 60°–70° N and (b) 60°–70° S. The dashed red lines represent one standard deviation of the ensemble-mean control simulation.

[24] These altered $NO_x$ levels have important consequences for the $O_3$ abundance. While the $O_3$ response is more complex, Figure 6 reveals strong positive anomalies in winter at mid and high latitudes, turning into weaker negative anomalies in the spring-summer (SH) or spring (NH). In both hemispheres, when sunlight returns to the polar regions in the spring, $NO_x$ and $O_3$ are also clearly anti-correlated between the 30–5 hPa pressure range, where the $NO_x$ catalytic cycle dominates (Figures 5a, 5b, 5e, and 5f). Below about 30 hPa, the $O_3$ increase is not accompanied by a negative anomaly in $NO_x$, but the change in the partitioning in $NO_y$ implicated by the anomaly in the $NO_x/NO_y$ ratio is indicative of a mitigating effect upon the halogen-induced $O_3$ depletion in this region.

### 3.3. Response in Zonal-Mean Winds and TEM Circulation

[25] The results above indicate that reaction (R1) leads to a weakened polar vortex during springtime. However, the origin of the zonal wind anomalies requires a careful analysis. This is further demonstrated in Figure 8, which shows the annual climatological cycle of zonal-mean zonal wind at 10 hPa averaged over the latitude band 60°–70°. The westerlies are weaker in the perturbed simulation during spring in the NH, and from winter to early summer in the SH. The zonal wind anomaly exceeds one standard deviation of the variability in the control simulation during July and November in the SH. These zonal wind decreases are not confined to the 10 hPa level, but rather extends throughout the entire stratosphere and lower mesosphere. This is demonstrated in Figure 9, which shows the monthly mean, ensemble-mean difference in zonally averaged zonal winds during the months where the zonal anomalies in Figure 8 are large, i.e., April–May in the NH and November–December in the SH. Overlaid are the corresponding zonal winds from the control simulation. In both hemispheres, these monthly mean negative wind anomalies are statistically significant, especially in late spring, at the 0.75 to 0.90 level depending on latitude or pressure. We now demonstrate that the weaker polar vortex in the perturbed run coexists with a stronger planetary wave forcing diagnosed by the EPFD, and with a stronger TEM circulation. To this end, the ensemble-mean TEM circulation differences between the two simulations are diagnosed alongside the meridional distributions of the long-lived tracer $N_2O$. In Figures 10a, 10c, 10e and 10g, we present the climatological seasonal latitude-height distributions of the relative differences between the two simulations for $N_2O$ (in percent and color shading). Note that small absolute differences in $N_2O$ can appear as large relative differences. The corresponding $N_2O$ distributions from the control simulation are overlaid as black contours. The corresponding TEM circulation is also overlaid as black vectors. The joint examination of the $N_2O$ and TEM cross-sections further illustrates the polar enhancement in $N_2O$ in the spring, as seen in the maps at 10 hPa (Figures 6a and 6b) and discussed in Section 3.2. In the SH, the enhancement started in winter and persisted during the summer season, before waning in the lower polar stratosphere, around 50 hPa, during the autumn season.

[26] Figures 10b, 10d, 10f and 10h show the difference in TEM circulation between the simulations, as vectors, as well as the difference in the EPFD in color shading. The largest differences in TEM are found in winter above 10 hPa, at midlatitudes in the NH and at mid or high latitudes in the SH. These differences correspond to a strengthening of the TEM circulation, which appears consistent with the negative (westward) anomaly in the EPFD. The strengthened circulation can only be attributed to forcing by planetary waves.

### 3.4. Link Between the $O_3$ and Dynamical Response

[27] The depth of the wind anomalies, extending throughout the stratosphere, the altitude of the largest incipient $O_3$ perturbations in autumn and early winter, near 10 hPa (Figure 5e) and the pronounced EPFD anomaly, all point toward amplification of planetary waves as being the lead factor.

[28] In winter, the $NO_x$ catalytic cycle can be active up to sub-polar latitudes, giving rise to zonally asymmetric $O_3$ anomalies in response to opposite anomalies in $NO_x$ (Figure 6). Recent work with chemistry-climate models has

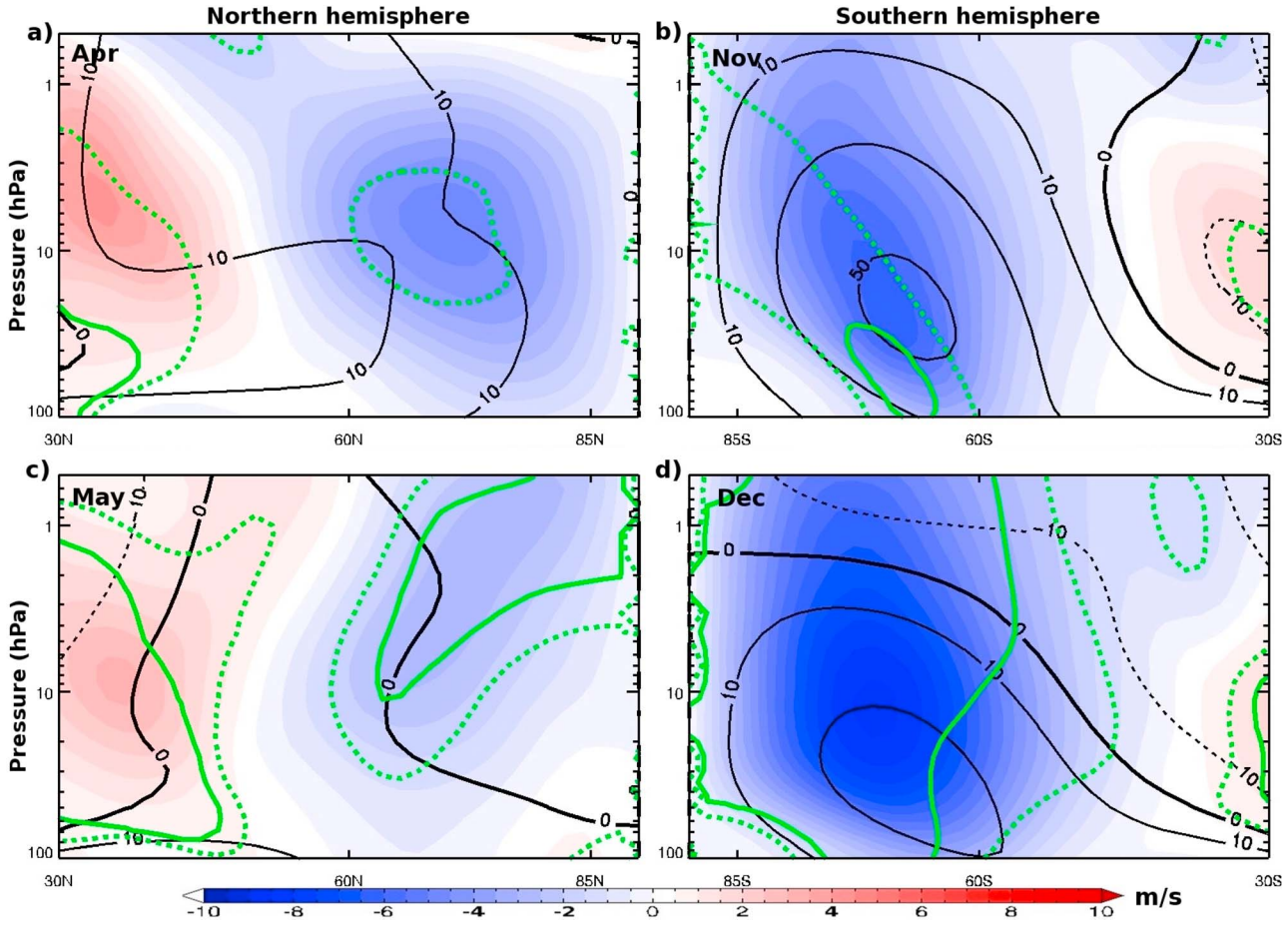


**Figure 9.** Monthly means ((a) April, (b) November, (c) May, (d) December) of the difference in the zonal-mean zonal wind as a function of latitude (30°–90°) and pressure (perturbed minus control, color shaded). Overlaid is the zonal-mean zonal wind from the control simulation (black contours, negative values dashed and the zero line is thicker). Significance at the 0.75 and 0.9 levels is indicated by dashed and solid green contours, respectively.

demonstrated that using radiatively active $O_3$ tends to alter the generation and propagation of planetary waves, with a strong influence on the circulation throughout the stratosphere, compared to simulations where only zonally averaged $O_3$ is used radiatively [*Kirchner and Peters*, 2003; *Gabriel et al.*, 2007; *Gillett et al.*, 2009; *Waugh et al.*, 2009; *McCormack et al.*, 2011]. While we compare here two fully coupled simulations, the perturbed run has a higher degree of zonal asymmetry in $O_3$. This is demonstrated in Figures 11a and 11b, which show the ensemble-mean climatological annual cycle of the standard deviation of ozone in the longitudinal direction at midlatitudes (30°S–60°S or 30°N–60°N), for the control simulation (dashed contours) and for the difference (perturbed minus control, color shading). In winter, the difference in the standard deviation is positive throughout the middle atmosphere in the SH, and above 10 hPa in the NH. This enhanced asymmetry in $O_3$ gives rise to short-wave heating anomalies, as demonstrated in Figures 11c and 11d at 10 hPa for the months of February (NH) and August (SH). The ozone ensemble-mean differences (color shading) are identical to those shown in Figure 6, but are shown here to be strongly correlated, as expected, to shortwave radiative heating rate anomalies, locally as high as 10%.

[29] It is not possible to fully disentangle the causality of the co-variability of planetary waves and $O_3$ resulting from multiple radiative-dynamical feedbacks between temperature and $O_3$. Neither was it possible even in the simpler case of comparing runs with $O_3$ fully coupled to the radiation to runs with only zonally symmetric $O_3$ radiatively active in papers cited above. Nevertheless, our diagnostics support the argument that the enhanced zonal asymmetries in $O_3$ induced by the initial $NO_x$ perturbations in winter middle and sub-polar latitudes would tend to amplify the planetary waves forcing leading to a strengthened TEM circulation, and a vortex that is significantly weakened earlier in the winter.

## 4. Further Discussion of Potential Biases in WACCM

[30] Sensitivity simulations with several different distributions of $H^+ \cdot (H_2O)_n$ have been completed (not shown), but failed to reproduce the polar $HNO_3$ enhancements reaching the stratopause, as observed in MLS (Figures 1 and 4) and SMR [*Orsolini et al.*, 2009] data. This failure appears to be due to a low bias in the climatological distribution of $N_2O_5$ in the upper stratosphere in WACCM, and does not

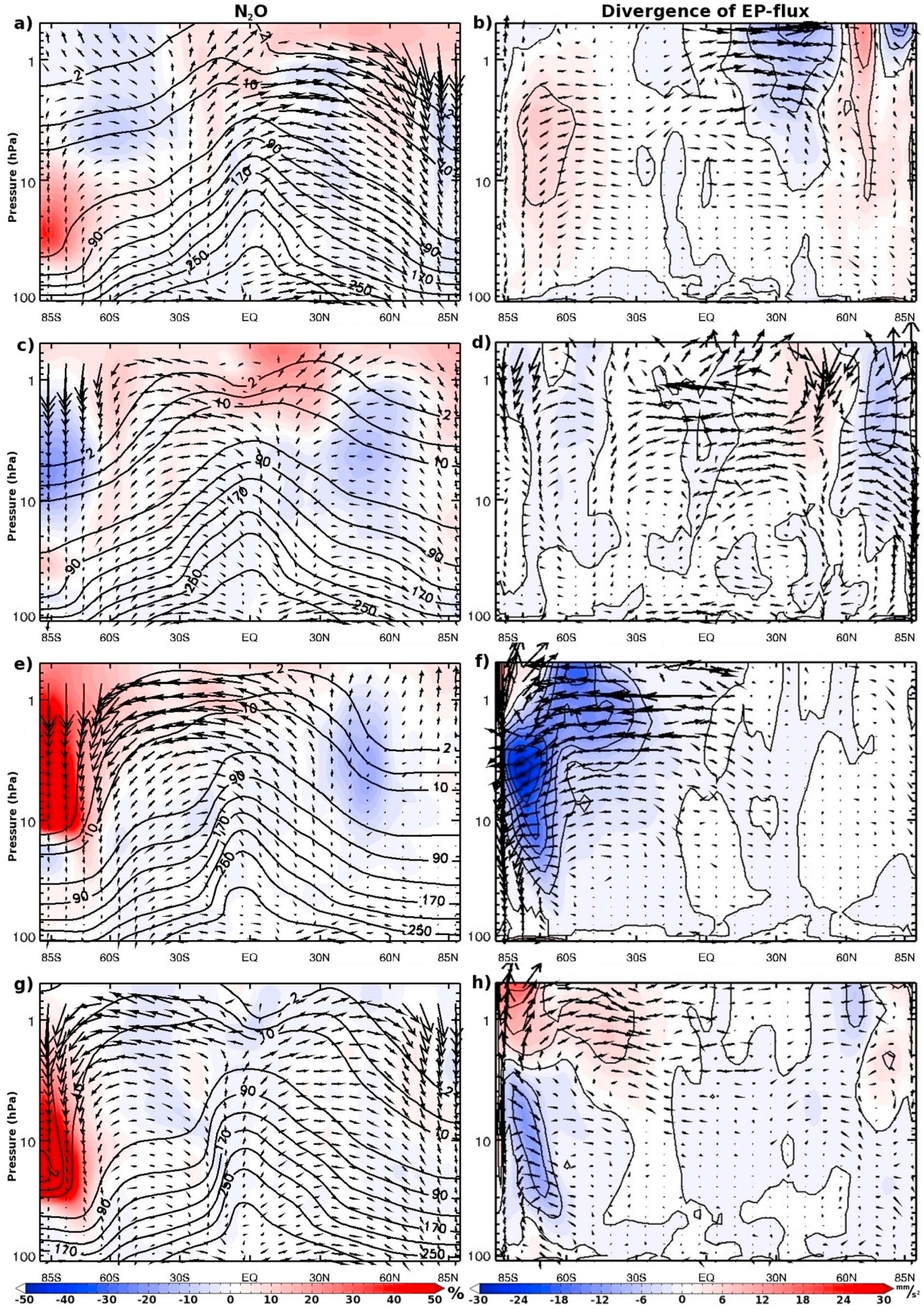
N2O
Divergence of EP-flux
a)
b)
c)
d)
e)
f)
g)
h)
Pressure (hPa)
1
10
100
85S
60S
30S
EQ
30N
60N
85N
2
10
90
170
250
-50 -40 -30 -20 -10 0 10 20 30 40 50 %
-30 -24 -18 -12 -6 0 6 12 18 24 30 mm/s2

**Figure 10**

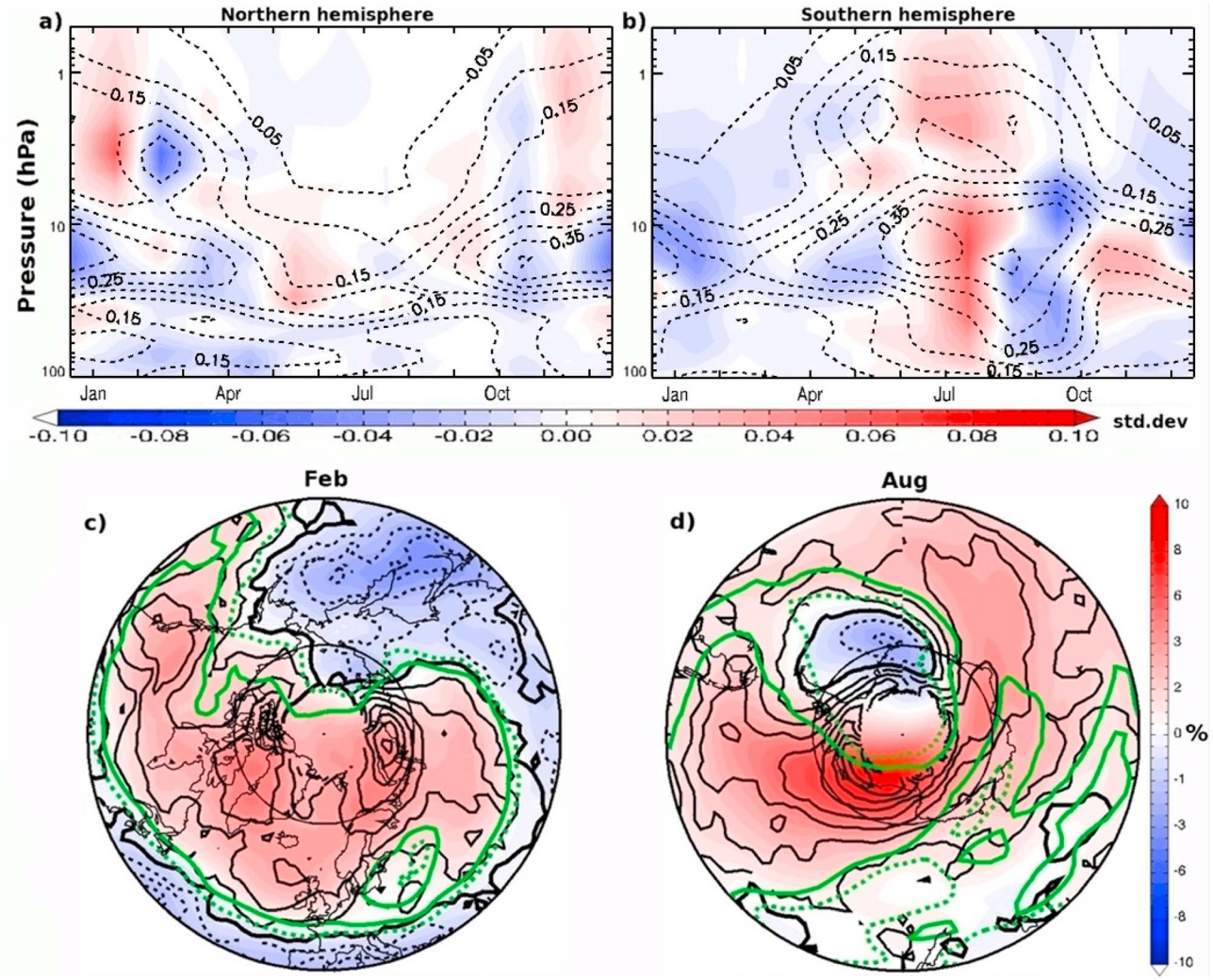


**Figure 11.** (a, b) Climatological annual cycle of the ensemble mean differences (perturbed minus control, color shaded) in the standard deviation for volume mixing ratio of $O_3$ (ppmv) in the longitudinal direction, averaged over the midlatitudes (30°–60°) in the northern and southern hemispheres. Overlaid as dashed contour lines are the corresponding fields in the ensemble-mean control simulation. (c, d) The climatological ensemble-mean relative difference (with respect to the control simulation, in % and color shaded) for $O_3$ at 10 hPa for February (NH) and August (SH). Overlaid as black contour lines are relative differences (in %) in the ensemble-mean shortwave radiative heating rates. Dashed and solid lines indicate negative and positive anomalies, respectively, with the zero line being thick; the contour interval is 1%. Significance at the 0.75 and 0.9 levels is indicated by dashed and solid green contours, respectively. The thin, solid, black circle is drawn at 70° in both hemispheres.

necessarily suggest that the observed $HNO_3$ enhancements originate from a different chemical processes. A comparison of the polar-averaged profile of $N_2O_5$ (>70° and DJF in the NH, >70° and MJJ in the SH) from both perturbed and control simulations together with MIPAS satellite observations is presented in Figure 12 (see Appendix A for more details about MIPAS data). It reveals a low bias in WACCM in the upper stratosphere, above the levels where the $HNO_3$ perturbations in Figure 3 have decayed, i.e., 3 hPa in the NH, and 6 hPa in the SH. Hence, the potential for $HNO_3$ production in the upper stratosphere is insufficient due to a too low abundance of $N_2O_5$ in WACCM. In the upper

**Figure 10.** (a, c, e, g) Meridional distributions of the ensemble mean differences (perturbed minus control, color shaded, in percent) in $N_2O$ for the DJF, MAM, JJA, and SON seasons. Overlaid as contour lines are the corresponding fields for the ensemble-mean control simulation, and as arrows is the TEM circulation also from the ensemble-mean control simulation. (b, d, f, h) Meridional distributions of the difference in the Eliassen-Palm flux divergence for the DJF, MAM, JJA, and SON seasons (color shaded). Overlaid as arrows is the difference in TEM circulation (perturbed minus control). Note that since the response in the TEM circulation is much smaller than the circulation itself, the vectors in the right column are not comparable in size to the vectors in the left column.

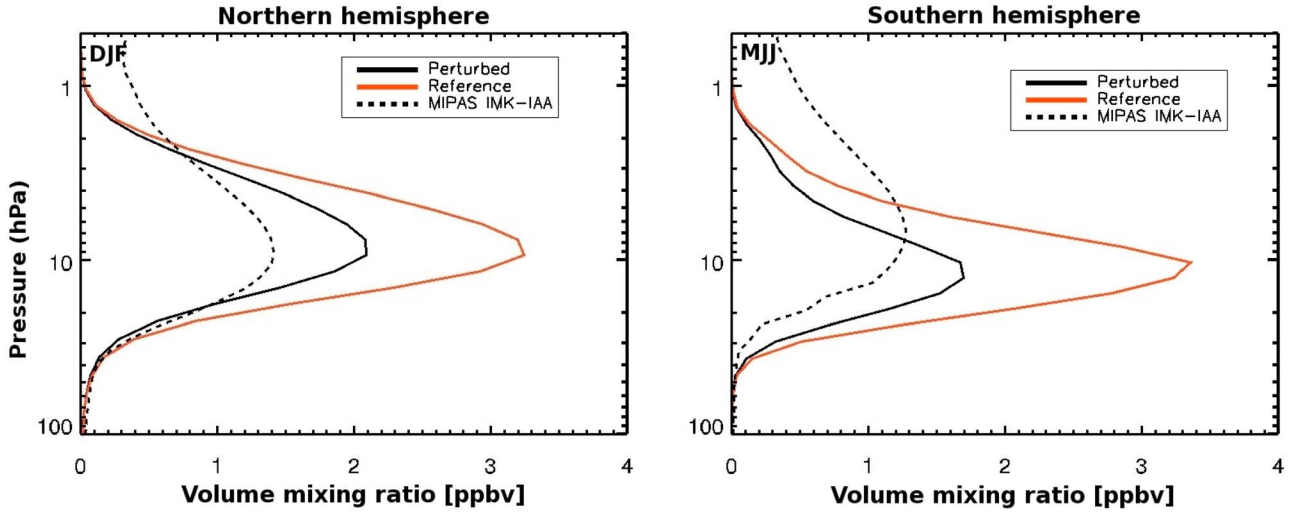


**Figure 12.** Vertical profiles of $N_2O_5$ (ppbv) for the DJF (NH) and MJJ (SH) seasons in the polar region (poleward of 70°) from the WACCM ensemble-mean perturbed simulation (solid black line), control simulation (solid red line) and MIPAS (dashed black line) data set (2007, 2008 and 2009).

stratosphere the use of an averaging kernel might help to reduce the differences between model and MIPAS observations. However, such a detailed comparison is beyond the scope of this study. Since the reaction that decomposes $N_2O_5$ is strongly dependent upon temperature, a warm model bias would cause the loss to be too large and hence a negative bias in $N_2O_5$. A temperature comparison with MIPAS (not shown) indeed reveals a warm bias in the upper stratosphere in WACCM. We also surmise that the source of $N_2O_5$, i.e., ultimately $NO_x$, is too low due to weak production from EPP or galactic cosmic rays. Another possibility is that the amount of $NO_x$ descending into the stratosphere might be underestimated in WACCM because the elevated levels of $NO_x$ created in the lower thermosphere do not reach the top of the descending branch of the TEM circulation [*Smith et al.*, 2011]. From the middle mesosphere down to the mid stratosphere, the TEM circulation is reasonably well captured in WACCM as demonstrated in the transport of carbon monoxide [*Kvissel et al.*, 2012]. Nevertheless, a further exploration of the causes of this upper stratospheric $N_2O_5$ deficit in WACCM is beyond the scope of this study. Below these levels, the high bias in the control run has been improved by the introduced $N_2O_5$ conversion through reaction (R1), and abundances of about 2 ppbv are closer to the MIPAS observations. In the middle stratosphere, the perturbed run still shows an excess of $N_2O_5$ that could be alleviated by a higher conversion rate to $HNO_3$ or a higher background abundance of hydrated ion clusters. We have chosen an idealized distribution of ion clusters, which is still poorly constrained by observations. The reaction rate $k_2$ and its potential dependence on cluster size could also be constrained by better experimental data.

[31] Another bias in these WACCM version 3.1.9 simulations concerns the anomalous persistence of the austral winter vortex into spring and early summer (e.g., Figures 8 or 9), which causes $O_3$ zonal anomalies in Figure 11 to be off phase with those in observations (*Gillett et al.*, 2009), and the downward TEM circulation in the lower stratosphere to excessively compress and lower the $N_2O$ contours (e.g., Figure 7).

## 5. Summary and Discussion

[32] In this paper, we have studied the WACCM response to the introduction of a chemical pathway that produces $HNO_3$ by conversion of $N_2O_5$ upon hydrated water clusters $H^+\cdot(H_2O)_n$. The current study is the first of its kind, where this chemical reaction is introduced in a free-running CCM. As such, it is exploratory, and a time-independent distribution of hydrated water clusters has been prescribed in the model simulations. We aim to improve our understanding of the EPP-$NO_x$ "indirect effect"; therefore, individual solar proton events are not included in the present study.

[33] We have used an ensemble approach, carrying out four pairs of control and perturbed simulations each lasting four years, and addressed the statistical significance of the results. The main focus has been on annually re-occurring chemical signatures in the polar regions. Despite the two model simulations being similar in all other aspects, it is not surprising that there are differences in the distributions of trace gases that can be attributed to changes in transport. The introduced chemical pathway for $HNO_3$ alters the internal partitioning of the $NO_y$ family during winter months in both hemispheres, and the perturbed $HNO_3$ ultimately impacts the distribution of $O_3$. Through $O_3$ changes, both temperature and dynamics are affected allowing for complex chemical-dynamical feedbacks lasting beyond the cold season when the reaction (R1) is active.

[34] Statistically significant changes in the climatological distributions of constituents from the nitrogen family or $O_3$ compared to the control run include: i) a cold season production and loss of $HNO_3$ and $N_2O_5$, respectively, ii) a cold season decrease and increase in $NO_x/NO_y$ ratio and $O_3$, respectively, in the polar regions of both hemispheres, and iii) a $NO_x$ and $N_2O$ polar increase in spring-to-summer in the SH, and in spring in the NH. Associated with the later (iii) is an $O_3$ decrease, which is only statistically significant in the SH.

[35] Through the inclusion of the ion cluster reaction, we see an improved seasonal evolution of modeled $HNO_3$ compared to satellite observations from MLS, esp. regarding the seasonal cycle in the polar mid-stratosphere. However, a prior overestimation at lower levels in the NH is worsened by implementing reaction (R1). The $N_2O$ distribution is also improved in the perturbed run compared to the MLS observations, esp. in the spring-to-summer in the SH. Our comparison of WACCM versus MLS observations also include $O_3$, shown in auxiliary material Figure S2, but discrepancies in the lower stratosphere in winter and spring are difficult to ascribe to this effect only and not to other model processes, such as the anomalous vortex persistence or heterogeneous chemistry on PSCs.

[36] The seasonal evolution of zonal-mean zonal winds and temperature is not identical in the two simulations, which we argue is caused by strengthened planetary waves induced by the midlatitude zonal asymmetries in $O_3$ and short-wave heating. The strengthening in the perturbed runs ultimately results from the influence of the $NO_x$ cold season deficit which leads to a higher degree of zonal asymmetry in $O_3$ at mid and sub-polar latitudes. In the SH, the weakening of the zonal-mean winds indeed begins in winter but is statistically most significant in late spring and summer, and in the NH, it is significant in the spring.

[37] The well-studied EPP-$NO_x$ "indirect" effect allows $O_3$ depletion in the spring through the catalytic $NO_x$ cycle [*Jackman et al.*, 2005, 2008; *Randall et al.*, 2006]. Our study uncovers a new way for the EPP-$NO_x$ "indirect" effect to be further amplified in a model. The springtime polar $NO_x$ increase arises from a weaker polar vortex that allows more transport of $N_2O$ polewards, instead of in situ production of $NO_x$. On the other hand, the WACCM biases, e.g., in $N_2O_5$, makes reaction (R1) ineffective above approximately 10 hPa, as shown in Figure 4. If WACCM would allow higher levels of $NO_x$ to reach the stratosphere from above [*Smith et al.*, 2011], the EPP-$NO_x$ "indirect" effect would yet be further amplified by the mechanism we propose here. As mentioned earlier, heterogeneous conversion of $N_2O_5$ into $HNO_3$ onto volcanic aerosols can also occur in the lower stratosphere [*Bekki et al.*, 1997], and the question arises whether analogous dynamical couplings would be at play when aerosol loading is large enough. The issues of $N_2O_5$ and dynamical biases in WACCM 3.1.9 make a compelling case for investigating the dynamical feedbacks of the reaction (R1) in other chemistry-climate models. Nevertheless, it is quite remarkable that the inclusion of this chemical pathway has changed the magnitude and the seasonal march of the stratospheric jet. Such change highlights the importance of $NO_x$ in modulating ozone abundances, and of EPP processes for the entire middle atmosphere.

## Appendix A

[38] In this study, we use the version 3.3 of Microwave Limb Sounder (MLS) L2 data. All the data were screened according to the instruction given in the MLS Data Quality and Description Document [*Livesey et al.*, 2011]. The MLS instrument is mounted on NASA Aura satellite, launched in 2004 into a sun-synchronous near-polar orbit. It measures the thermal emission of more than 15 trace species in the microwave range, in both day and night conditions, covering latitudes up to 82° on each orbit. These measurements can be inverted into altitude profiles with a range between 215 and 0.01 hPa (≈10–80 km). The quality of the data varies considerably depending upon the height of the retrieval and the component retrieved. For $HNO_3$, the standard recommended altitude range is between 215 and 1.5 hPa (≈10–50 km) [*Livesey et al.*, 2011, chapter 3.11]. The vertical resolution in the middle/upper stratosphere is 4–5 km up to about 1 hPa, where it starts to degrade rapidly down to 12 km around 0.1 hPa. Retrieved mixing ratios at 1 hPa are also scientifically useful during episodes when production of $HNO_3$ increases and the signal-to-noise ratio improves. These episodes can for instance happen during strong solar proton events [*Verronen et al.*, 2008, 2011], or during winters when an enhanced downward circulation advects $NO_x$-rich air from the mesosphere into the stratosphere.

[39] We have also used 3 years of $N_2O_5$ observations by MIPAS over the years 2007–2009. The MIPAS IMK-IAA data set from the Institute for Meteorology and Climate Research has been used (Atmospheric Trace Gases and Remote Sensing website: http://www.imk-asf.kit.edu). We have used the visibility flag and the averaging kernel (values less than 0.03 is removed) to remove bad data and data gaps.

[40] **Acknowledgments.** O.K.K., Y.O.R. and F.S. were supported by the Norwegian Research Council NORKLIMA program (Project Arctic_Lis, project number #178629). O.K.K. has had a three-week stay at NCAR supported by The Norwegian Research School in Climate Dynamics (ResClim). Work at the Jet Propulsion Laboratory, California Institute of Technology, was done under contract with NASA. The authors would like to acknowledge Varavut Limpasuvan and Amund Søvde for useful comments.

## References

Austin, J., R. R. Garcia, J. M. Russell III, S. Solomon, and A. F. Tuck (1986), On the atmospheric photochemistry of nitric acid, *J. Geophys. Res.*, *91*(D5), 5477–5485, doi:10.1029/JD091iD05p05477.

Beig, G., S. Walters, and G. Brasseur (1993), A two-dimensional model for ion composition in the stratosphere: 1. Positive ions, *J. Geophys. Res.*, *98*, 12,767–12,773, doi:10.1029/93JD00881.

Bekki, S., M. Chipperfield, J. Pyle, J. Remedios, S. Smith, R. Grainger, A. Lambert, J. Kumer, and J. Mergenthaler (1997), Coupled aerosol-chemical modeling of UARS $HNO_3$ and $N_2O_5$ measurements in the Arctic upper stratosphere, *J. Geophys. Res.*, *102*(D7), 8977–8984, doi:10.1029/96JD03130.

Böhringer, H., D. Fahey, F. C. Fehsenfeld, and E. E. Ferguson (1983), The role of ion-molecule reactions in the conversion of $N_2O_5$ to $HNO_3$ in the stratosphere, *Planet. Space Sci.*, *31*(2), 185–191, doi:10.1016/0032-0633(83)90053-3.

Brasseur, G. P., D. A. Hauglustaine, S. Walters, R. J. Rasch, J.-F. Müller, C. Granier, and X. X. Tie (1998), MOZART, a global chemical transport model for ozone and related chemical tracers: 1. Model description, *J. Geophys. Res.*, *103*(D21), 28,265–28,289, doi:10.1029/98JD02397.

Callis, L. B., and J. D. Lambeth (1998), $NO_y$ formed by precipitating electron events in 1991 and 1992: Descent into the stratosphere as observed by ISAMS, *Geophys. Res. Lett.*, *25*(11), 1875–1878, doi:10.1029/98GL01219.

de Zafra, R., and S. P. Smyshlyaev (2001), On the formation of $HNO_3$ in the Antarctic mid to upper stratosphere in winter, *J. Geophys. Res.*, *106*, 23,115–23,125, doi:10.1029/2000JD000314.

de Zafra, R. L., V. Chan, S. Crewell, C. Trimble, and J. M. Reeves (1997), Millimeter wave spectroscopic measurements over the South Pole: 3. The behavior of stratospheric nitric acid through polar fall, winter, and spring, *J. Geophys. Res.*, *102*(D1), 1399–1410, doi:10.1029/95JD03679.

Gabriel, A., D. Peters, I. Kirchner, and H.-F. Graf (2007), Effect of zonally asymmetric ozone on stratospheric temperature and planetary wave propagation, *Geophys. Res. Lett.*, *34*, L06807, doi:10.1029/2006GL028998.

Garcia, R. R., D. R. Marsh, D. E. Kinnison, B. A. Boville, and F. Sassi (2007), Simulation of secular trends in the middle atmosphere, 1950–2003, *J. Geophys. Res.*, *112*, D09301, doi:10.1029/2006JD007485.

Gille, J. C., et al. (1984), Accuracy and precision of the nitric acid concentrations determined by the Limb Infrared Monitor of the Stratosphere

Experiment on NIMBUS 7, *J. Geophys. Res.*, *89*(D4), 5179–5190, doi:10.1029/JD089iD04p05179.

Gillett, N. P., J. F. Scinocca, D. A. Plummer, and M. C. Reader (2009), Sensitivity of climate to dynamically consistent zonal asymmetries in ozone, *Geophys. Res. Lett.*, *36*, L10809, doi:10.1029/2009GL037246.

Jackman, C. H., M. T. DeLand, G. J. Labow, E. L. Fleming, D. K. Weisenstein, M. K. W. Ko, M. Sinnhuber, J. Anderson, and J. M. Russell (2005), The influence of the several very large solar proton events in years 2000–2003 on the neutral middle atmosphere, *Adv. Space Res.*, *35*, 445–450, doi:10.1016/j.asr.2004.09.006.

Jackman, C. H., et al. (2008), Short- and medium-term atmospheric constituent effects of very large solar proton events, *Atmos. Chem. Phys.*, *8*, 765–785, doi:10.5194/acp-8-765-2008.

Kawa, S. R., J. B. Kumer, A. R. Douglass, A. E. Roche, S. E. Smith, F. W. Taylor, and D. J. Allen (1995), Missing chemistry of reactive nitrogen in the upper stratospheric polar winter, *Geophys. Res. Lett.*, *22*(19), 2629–2632, doi:10.1029/95GL02336.

Kinnison, D. E., et al. (2007), Sensitivity of chemical tracers to meteorological parameters in the MOZART-3 chemical transport model, *J. Geophys. Res.*, *112*, D20302, doi:10.1029/2006JD007879.

Kinnison, D. E., et al. (2008), Global observations of $HNO_3$ from the High Resolution Dynamics Limb Sounder (HIRDLS): First results, *J. Geophys. Res.*, *113*, D16S44, doi:10.1029/2007JD008814.

Kirchner, I., and D. Peters (2003), Modelling the wintertime response to upper tropospheric and lower stratospheric ozone anomalies over the North Atlantic and Europe, *Ann. Geophys.*, *21*, 2107–2118, doi:10.5194/angeo-21-2107-2003.

Kvissel, O.-K., Y. J. Orsolini, F. Stordal, V. Limpasuvan, D. Marsh, and J. H. Richter (2012), Mesospheric intrusion and anomalous chemistry during and after a major stratospheric sudden warming, *J. Atmos. Sol. Terr. Phys.*, *78–79*, 116–124, doi:10.1016/j.jastp.2011.08.015.

Livesey, N. L., et al. (2011), Version 3.3 Level 2 data quality and description document, *Tech. Rep. JPL D33509*, Jet Propul. Lab., Pasadena, Calif. [Available at http://mls.jpl.nasa.gov.]

López-Puertas, M., B. Funke, S. Gil-López, T. von Clarmann, G. P. Stiller, M. Höpner, S. Kellmann, G. M. Tsidu, H. Fischer, and C. H. Jackman (2005), $HNO_3$, $N_2O_5$, and $ClONO_2$ enhancements after the October–November 2003 solar proton events, *J. Geophys. Res.*, *110*, A09S44, doi:10.1029/2005JA011051.

Manney, G. L., et al. (2008), The evolution of the stratopause during the 2006 major warming: Data and assimilated meteorological analyses, *J. Geophys. Res.*, *113*, D11115, doi:10.1029/2007JD009097.

McCormack, J. P., T. R. Nathan, and E. C. Cordero (2011), The effect of zonally asymmetric heating on the Northern Hemisphere winter polar stratosphere, *Geophys. Res. Lett.*, *38*, L03802, doi:10.1029/2010GL045937.

McDonald, M., R. L. de Zafra, and G. Muscari (2000), Millimeter wave spectroscopic measurements over the South Pole: 5. Morphology and evolution of $HNO_3$ vertical distribution, 1993 versus 1995, *J. Geophys. Res.*, *105*(D14), 17,739–17,750, doi:10.1029/2000JD900120.

Orsolini, Y. J., G. L. Manney, M. L. Santee, and C. E. Randall (2005), An upper stratospheric layer of enhanced $HNO_3$ following exceptional solar storms, *Geophys. Res. Lett.*, *32*, L12S01, doi:10.1029/2004GL021588.

Orsolini, Y. J., J. Urban, and D. P. Murtagh (2009), Nitric acid in the stratosphere based on Odin observations from 2001 to 2009–Part 2: High-altitude polar enhancements, *Atmos. Chem. Phys.*, *9*, 7045–7052, doi:10.5194/acp-9-7045-2009.

Orsolini, Y. J., J. Urban, D. P. Murtagh, S. Lossow, and V. Limpasuvan (2010), Descent from the polar mesosphere and anomalously high stratopause observed in 8 years of water vapor and temperature satellite observations by the Odin Sub-Millimeter Radiometer, *J. Geophys. Res.*, *115*, D12305, doi:10.1029/2009JD013501.

Randall, C. E., V. L. Harvey, C. S. Singleton, P. F. Bernath, C. D. Boone, and J. U. Kozyra (2006), Enhanced $NO_x$ in 2006 linked to strong upper stratospheric Arctic vortex, *Geophys. Res. Lett.*, *33*, L18811, doi:10.1029/2006GL027160.

Randall, C. E., V. L. Harvey, D. E. Siskind, J. France, P. F. Bernath, C. D. Boone, and K. A. Walker (2009), $NO_x$ descent in the Arctic middle atmosphere in early 2009, *Geophys. Res. Lett.*, *36*, L18811, doi:10.1029/2009GL039706.

Reddmann, T., R. Ruhnke, S. Versick, and W. Kouker (2010), Modeling disturbed stratospheric chemistry during solar-induced $NO_x$ enhancements observed with MIPAS/ENVISAT, *J. Geophys. Res.*, *115*, D00I11, doi:10.1029/2009JD012569.

Santee, M. L., G. L. Manney, N. J. Livesey, and W. G. Read (2004), Three-dimensional structure and evolution of stratospheric $HNO_3$ based on UARS Microwave Limb Sounder measurements, *J. Geophys. Res.*, *109*, D15306, doi:10.1029/2004JD004578.

Semeniuk, K., V. I. Fomichev, J. C. McConnell, C. Fu, S. M. L. Melo, and I. G. Usoskin (2011), Middle atmosphere response to the solar cycle in irradiance and ionizing particle precipitation, *Atmos. Chem. Phys.*, *11*, 5045–5077, doi:10.5194/acp-11-5045-2011.

Smith, A. K., R. R. Garcia, D. R. Marsh, and J. H. Richter (2011), WACCM simulations of the mean circulation and trace species transport in the winter mesosphere, *J. Geophys. Res.*, *116*, D20115, doi:10.1029/2011JD016083.

Stiller, G. P., et al. (2005), An enhanced $HNO_3$ second maximum in the Antarctic midwinter upper stratosphere 2003, *J. Geophys. Res.*, *110*, D20303, doi:10.1029/2005JD006011.

Urban, J., M. Pommier, D. P. Murtagh, M. L. Santee, and Y. J. Orsolini (2009), Nitric acid in the stratosphere based on Odin observations from 2001 to 2009–Part 1: A global climatology, *Atmos. Chem. Phys.*, *9*, 7031–7044, doi:10.5194/acp-9-7031-2009.

Verronen, P. T., B. Funke, M. López-Puertas, G. P. Stiller, T. von Clarmann, N. Glatthor, C.-F. Enell, E. Turunen, and J. Tamminen (2008), About the increase of $HNO_3$ in the stratopause region during the Halloween 2003 solar proton event, *Geophys. Res. Lett.*, *35*, L20809, doi:10.1029/2008GL035312.

Verronen, P. T., M. L. Santee, G. L. Manney, R. Lehmann, S.-M. Salmi, and A. Seppala (2011), Nitric acid enhancements in the mesosphere during the January 2005 and December 2006 solar proton events, *J. Geophys. Res.*, *116*, D17301, doi:10.1029/2011JD016075.

Waugh, D. W., L. Oman, P. A. Newman, R. S. Stolarski, S. Pawson, J. E. Nielsen, and J. Perlwitz (2009), Effect of zonal asymmetries in stratospheric ozone on simulated Southern Hemisphere climate trends, *Geophys. Res. Lett.*, *36*, L18701, doi:10.1029/2009GL040419.